FULL PAPER

XAFS and DFT Characterisation of Protonated Reduced Fe Hydrogenase Analogues and Their Implications for Electrocatalytic Proton Reduction

Mun Hon Cheah[a,b] and Stephen P. Best*[a]

The relationship between the structures of reduced, protonated diiron compounds relevant to the diiron subsite of the Fe-hydrogenase H cluster, $[2Fe]_H$, and the rate of electrocatalytic proton reduction is explored by a combination of experimental and computational approaches. Analysis of the X-ray absorption fine structure (XAFS) of the two-electron, two-proton product of $[Fe(CO)_3]_2(\mu\text{-PPh}_2)_2$ (**DP**) shows distortions of the primary coordination environment of the Fe centre that result from the *trans* influence of the terminally bound hydrido ligand. The difference in Fe–C(O) bond lengths for the CO groups *cis* and *trans* to the hydrido ligand is similarly predicted by density functional theory, although there is relatively poor agreement between the magnitude of the difference obtained by XAFS and DFT methods. The calculated energies of the *cis* and *trans* stereoisomers of **DP**-H_2 with both hydrido ligands normal to the FeP2 plane (axial:axial)

are within 0.5 kcal mol^{-1} of each other and lower, by approximately 4.5 kcal mol^{-1}, than those of the axial:equatorial isomer. Similar trends in the relative energies are found for the hydrido forms of $[Fe(CO)_3]_2[\mu\text{-PhP(CH}_2)_3\text{PPh}]$ (**3P**). The rates of dihydrogen elimination from **3P**-H_2 and analogues with ethanedithiolate and propanedithiolate bridging ligands (**2S**-H_2 and **3S**-H_2) have been re-evaluated by using recent DFT calculations of equilibrium constants and reduction potentials. The rate constants 4–8, 2–7 and 1.5–4 s^{-1} for dihydrogen elimination from the two-electron, two-proton analogues of **2S**, **3S** and **3P**, respectively, for reactions conducted with *p*-toluenesulfonic acid fall within a narrow range and are consistent with reactions following a similar path but inconsistent with the different transition states proposed for dihydrogen elimination from **2S**-H_2 and **3S**-H_2.

Introduction

The iron carbonyl cyanide moiety at the catalytic centre of each of the structurally distinct types of hydrogenase has spawned a broad range of experimental and computational investigations driven by the promise of efficient hydrogen activation catalysts based on abundant chemical feedstocks.[1] Ultimately, the imperative of such a discovery is the advantage that dihydrogen provides as an energy vector for energy storage and use. Despite the deceptive simplicity of the metal cofactors and the rapid advances toward structural analogues of the diiron subsite of the [FeFe] hydrogenase H-cluster, $[2Fe]_H$, which exhibit some of the electrocatalytic properties of the enzyme,[2] none of the systems so far reported[3] facilitate rapid, efficient (low overpotential) electrocatalysis and are not robust in terms of their operation in the presence of dioxygen. This contribution is concerned with the relationship between the protonated, reduced diiron carbonyl intermediates and the reaction rate.

Specifically, we explore the markedly different reactivity of terminally bound iron hydride species with respect to dihydrogen elimination following protonation and review modelling of the electrocatalytic proton reduction response in light of the energetics of the calculated intermediates.

For all the analogues of $[2Fe]_H$ other than $[Fe_2(\mu\text{-SCH}_2)_3\text{-C(CH}_3)(CO)_4]_2$ (**4Fe6S**), turnover at the two-electron level proceeds at a much slower rate than the enzymatic reaction.[4] It was proposed that the high reactivity of **4Fe6S** be associated with a reaction path involving a terminally bound hydride (Figure 1a), a suggestion in keeping with more detailed DFT calculations[5] together with the differences in reactivity of the isomeric forms of $[\{FeH(PMe_3)_2\}\text{-}\{Fe(CO)(PMe_3)_2\}\{\mu\text{-S(CH}_2)_2\text{S}\}\mu\text{-CO}]^+$ (**A**-H_t^+) (Figure 1b).[6] However, it is also clear that terminally bound hydrides are not sufficient for high electrocatalytic reactivity; the closely related complex $[\{Fe(CO)(PPh_2\text{-CHCHPPh}_2)\}_2\{\mu\text{-S(CH}_2)_2\text{S}\}]$ can be protonated by $HBF_4\cdot Et_2O$ to give a terminally bound hydride as the kinetic product, but does not turnover on protons without further reduction.[7]

More generally, electron-rich dithiolate-bridged diiron(I) carbonyl–phosphane compounds are Brønsted bases and give bridged hydrides as stable products,[8] although terminally bound hydrides may be identified particularly when the coordination environments are different about the iron centres, for example, $[Fe(CO)_3][Fe(CO)\{Ph_2P(CH_2)_2\text{-}$

[a] School of Chemistry, University of Melbourne,
Victoria 3010, Australia
Fax: 61-3-93475180
E-mail: spbest@unimelb.edu.au
[b] Australian Beamline, Photon Factory KEK 1-1 Oho,
Tsukuba, Ibaraki 305-0801, Japan
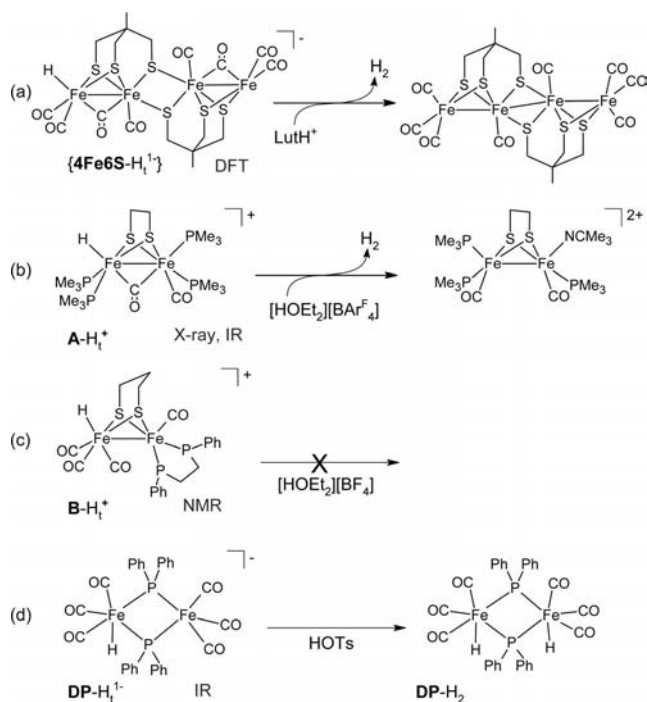Fax: +81-29-864-7967
E-mail: cheah@anbf2.kek.jp

Figure 1. Structures of diiron compounds proposed to include a terminal hydride together with the evidence for the proposed structure and the reactions with acids. Reactions (a) to (c) were conducted in CH_2Cl_2, and (d) has been reported in THF. Labels for the structures deduced from DFT calculation are enclosed in parentheses.

PPh_2}]{μ-S(CH$_2$)$_3$} (**B**).[9] However, these protonated forms must be reduced to provide a driving force for dihydrogen elimination. Hence, the stability of **B**-H$_t^+$ in the presence of acid is due to thermodynamic and not kinetic considerations. A clear example of a related terminally bound iron hydride that is unreactive, despite having a large thermodynamic driving force for protonation and dihydrogen elimination, is the singly protonated form of [[Fe(CO)$_3$]$_2$(μ-PPh$_2$)$_2$]$^{2-}$, **DP**$^{2-}$.[10] In this case protonation occurs at the remote iron to give **DP**-H$_2$ with no observable elimination of dihydrogen even when the reaction is conducted in the presence of a large excess of acid (Figure 1d). The first part of the paper will focus on experimental and computational examination of the structures of **DP**-H$_2$ and **DP**-H^{1-} in the context of the kinetic barrier to protonation of the latter species to give dihydrogen elimination.

Detailed computational analysis of the reaction path of electrocatalytic proton reduction by an analogue of [Fe]$_H$ hydrogenase H-cluster with strong acids was first based on [Fe(CO)$_3$]$_2$|μ-S(CH$_2$)$_3$S, (**3S**).[11] More recent studies include the ethanedithiolate analogue, **2S**,[12] and the tetrairon compound **4Fe6S**.[5] Additionally, calculations of the intermediate species generated during electrocatalytic proton reduction of acetic acid by the benzenedithiolate-bridged analogue, **BDT**,[13] and [Fe(CO)$_3$]$_2${μ-PhP(CH$_2$)$_3$PPh} (**3P**) have been reported.[14] The reaction path calculated for **3S** was grounded by the extensive electrochemical and spectroscopic information available for the compound and dif-

ferent electrogenerated products.[15] In this case, turnover at the two-electron/two-proton level proceeds by an ECEC′ path where the "E" steps involve one-electron redox reactions and the "C" steps correspond to single-proton transfers (with structural rearrangement). The catalyst is regenerated by rate-limiting dihydrogen elimination. DFT analysis suggests that the 1e/1H$^+$ species, which features a hydride bridging the Fe–Fe bond,[11] a proposition accordant with the extensive X-ray crystallographic evidence primarily from electron-rich phosphane-substituted analogues.[8d] The structure of the productive 2e/2H$^+$ intermediate is more contentious. For **3S**, the DFT calculations of DeGioia and co-workers suggest a dihydride, {**3S**-H$_2$} (Scheme 2) with an H–H distance below 2 Å.[16] The transition state leading to dihydrogen elimination was located for a structure in which dihydrogen asymmetrically bridges the two iron centres. In addition, the transition state is stabilised by a rearrangement of the alkyl chain of the propanedithiolato bridging ligand, {**3S**-H$_2$‡}.[3b–3d,17] More recent calculations of **2S** by Hall and co-workers failed to locate a transition state leading to dihydrogen elimination from the analogous intermediate of {**3S**-H$_2$}, and the proposed reaction pathway was considered most likely to proceed through intermediate {**2S**-H$_2$} with transition state {**2S**-H$_2$‡}.[12] The similar electrocatalytic response for proton reduction by **2S** and **3S**, including the rate of dihydrogen elimination from the 2e/2H$^+$ adduct, appears to be at odds with reaction paths that proceed through intermediates of markedly different structure. The calculated equilibrium constants and pK_a values for the intermediate species allow for a more tightly constrained modelling of the electrocatalytic response and evaluation of the relationship between the rate of dihydrogen elimination and the geometry of the intermediate species.

Results and Discussion

XAFS of DP-H$_2$

While we have not been successful in obtaining crystalline samples of **DP**-H$_2$, well-defined solutions suitable for XAFS analysis could be prepared by mixing solutions of chemically or electrochemically generated **DP**$^{2-}$ and an excess of *p*-toluenesulfonic acid (HOTs). The quality of structural information that can be extracted from the XAFS analysis depends on the extent of the useful data, and this depends on the quality of the sample and the characteristics of the beamline. In addition to chemical factors, the quality of the sample is affected by the presence of crystallites, most likely solvent, formed during freeze-quenching. Bragg diffraction from randomly oriented crystallites gives strong signals at different energies for the different detector elements and can compromise a high proportion of the measured fluorescence data. While it is an excellent electrochemical solvent, acetonitrile has a tendency to form microcrystals on freezing, and this, together with the characteristics of the BL20B beamline, have allowed collection of good quality XAFS up to a *k* value of 13.5 Å^{-1}. When the *R*

range is taken into account, this translates into an effective information content of 25 independent points.[18] Accordingly, the XAFS is modelled in terms of structures that include the minimum number of inequivalent scatters. Since the scattering amplitude depends both on the absorber–scatter distance and the atomic number of the scattering atom, the contribution to the XAFS from direct scattering interactions involving the hydrogen atom may be insignificant. For this reason, models that include and exclude the Fe–H group were examined.

The model used to analyse the XAFS data is shown in Figure 2. Protonation of the planar 2Fe2P core is expected to give an octahedral Fe centre in which the hydrogen atom is placed in an axial position, that is, normal to the 2Fe2P plane. This gives the more preferred facial stereochemistry for the iron tricarbonyl fragments. The population of the scattering atom is adjusted to give the averaged coordination of the two equivalent iron atoms. This has the effect of increasing the weighting of the bridging phosphido groups relative to the molecular formula. By application of geometrical constraints, this gives seven unique non-hydrogen atoms each requiring one positional and one Debye–Waller variable, which, together with E^0 and S_0^2, give a total of 16 variables. Refinements were carried out by using data in the k and R ranges of 1–13.5 Å^{-1} and 1–4 Å, respectively. The number of multiple scattering paths and the maximum calculated path length were both limited to 4 to model the Fe–C–O interactions. In order to assess whether the scattering interactions associated with the low-atomic-number hydrogen atoms impact significantly on the XAFS, the data for **DP**-H$_2$ and **DP**$^{2-}$ were analysed with and without inclusion of H atoms. Initially, the number of parameters for the refinements were held constant by fixing the Fe–H distance and the Debye–Waller factor for the H atom to values of 1.40 Å and 0.0010 Å^2, respectively, where the former is at the lower limit of the X-ray-determined Fe–H distances[19] and the latter is within the range commonly found for light scattering atoms. Refinement of the XAFS data was well-behaved, and the observed and calculated XAFS and Fourier transform are given in Figure 3. The refinement statistics and final parameters are summarised in Table 1.
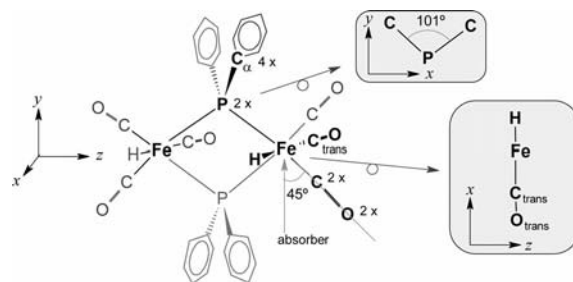
Figure 2. Structural model used for XAFS analysis. The molecule is treated as having C_{2v} symmetry with the H atoms in axial positions. Only the carbon atoms of the phenyl ring bound to the phosphorus atom are included in the model. The atoms that are related by symmetry are shown with a grey background.
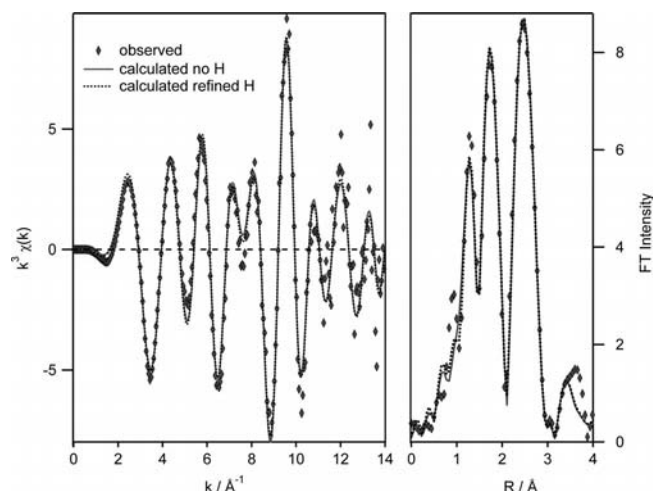
Figure 3. XAFS and associated Fourier transform derived from X-ray absorption spectra of freeze-quenched CH$_3$CN solutions of **DP**-H$_2$ (ca. 10 K) together with the calculated functions based on the refined parameters given in Table 1.

Despite the restrictions on a number of the geometric degrees of freedom of the scattering atoms, the simple models allow the main features of the XAFS data to be reproduced with good fidelity, this being well illustrated by the observed and calculated Fourier transform, which corre-

Table 1. Final refinement statistics and parameters for **DP**-H$_2$.

Parameter[a]	**DP**-H$_2$		**DP**$^{2-}$	
	pop(H)[b] = 0	pop(H) = 1	pop(H)[b] = 0	pop(H) = 1
$\chi^{2[c]}$	2.11	1.68	1.99	1.37
R_{XAFS}/%[c]	13.22	11.80	11.09	9.21
E_0/eV {S_0^2}	–8.30 {0.84}	–8.64 {0.90}	–7.19 {0.91}	–7.59 {0.90}
Fe–Fe	3.62 (3.2)[d]	3.62 (3.4)	3.56 (3.6)	3.57 (3.7)
Fe–μ-**P**	2.26 (4.8)	2.26 (5.3)	2.26 (2.8)	2.26 (2.7)
Fe–**C**(O)	1.75 (0.9)	1.75 (0.9)	1.76 (1.0)	1.74 (1.5)
C–**O**	1.17 (1.1)	1.18 (1.4)	1.14 (1.3)	1.16 (1.4)
P–**C**$_\alpha$	1.88 (1.3)	1.88 (1.4)	1.90 (8.5)	1.91 (6.0)
Fe–**C**$_{trans}$(O)	1.83 (1.4)	1.84 (1.0)	1.72 (2.7)	1.76 (1.0)
C$_{trans}$–**O**$_{trans}$	1.16 (3.3)	1.15 (5.5)	1.28 (3.3)	1.23 (3.9)
Fe–**H**	–	1.4[e] (1.0)[e]	1.4[e] (1.0)[e]	

[a] Distances given in Å. [b] Population of the hydrogen scattering atom. [c] Definitions of χ^2 and R_{XAFS} are given in ref.[10], the k and R range for data analysis were 1–13.5 Å^{-1} and 1–4 Å, respectively. [d] The bond length uncertainty is estimated to be 0.02 Å[20] and $10^3 \times$ Debye–Waller/Å^2 for the scattering atom (bold) is given in parentheses. [e] Parameter fixed during the refinement.

spond to a radial distribution function offset by approximately 0.5 Å due to a phase shift of the scattered photoelectron wave. The poorer agreement between the calculated and observed results is obtained for distances larger than 3.5 Å. This observation is readily explained in terms of the assumption that only the carbon bound directly to the phosphorus atom of the diphenylphosphido bridge need be included in the model. Since contributions to the XAFS from scattering atoms at such long distances are not likely to affect significantly the comparison of models of the short Fe–H interaction, no further elaboration of the treatment of the phenyl groups was conducted.

Comparison of the XAFS calculated with the population assigned to the scattering H atom, pop(H), equal either to zero or one are indistinguishable aside from the region with R close to 1 Å (Figure 3), and this is reflected by the small change in the refinement statistics and in the absence of significant changes in the other structural parameters (Table 1). It is significant to note that similar improvements in refinement statistics are obtained from modelling the XAFS of DP^{2-} and DP-H_2 by inclusion of an Fe–H interaction in the model despite the absence of such a group for DP^{2-}. Clearly, the contribution to the XAFS from the hydride groups is not of a sufficient magnitude to allow unambiguous identification of the Fe–H groups.

The XAFS refined structures of DP^{2-} and DP-H_2 reveal that protonation results in only minor changes in the Fe–Fe and Fe–P distances but a significant variation in the Fe–C(O) distances for the carbonyl groups *cis* and *trans* to the apical hydride. Since hydride is a ligand with a strong *trans* influence, the Fe–C$_{trans}$(O) distance would be expected to be the longer if the product is predominantly of the form with an apical hydride as shown in Figure 2. In accordance with these arguments, the Fe–C$_{trans}$(O) distance is 0.09 Å longer than Fe–C(O) length. Despite the limited direct structural information available for the Fe–H interaction from the XAFS analysis, the strong *trans* influence of the ligand results in significant secondary effects in the coordination environment of the Fe atom, which can be quantified by XAFS and can be used to obtain important insights into the stereochemistry and electronic interactions within the complex.

DFT Calculations

While the structural details of DP^{2-} have been determined crystallographically,[21] limited structural information is available from the XAFS of DP-H_2, and only IR spectra of DP-H^{1-} can be used to anchor the computational results. For the protonated compounds, different isomeric forms are possible, and the structural parameters, relative computed energies and spectroscopic signatures may be compared with experimental results. To distinguish between experimentally observed species and those obtained in *silico*, the computed species corresponding to local minima (based on analysis of the vibrational modes) are enclosed in parentheses; the computed structure of DP^{2-} is designated

$\{DP^{2-}\}$. The starting geometry of DP^{2-} is based on the crystallographic structure. The phenyl groups on the phosphido bridge are replaced by methyl groups. This simplification allows the calculations to reach convergence in a shorter time period, and the calculated structure of DP^{2-} is in good agreement with crystallographic results. A similar outcome is reported in an independent DFT study of DP and DP^{2-}.[22]

The starting geometry for calculation of DP-H^{1-} is based on the structure of $\{DP^{2-}\}$, in which a single H atom is placed on one of the Fe centres, and the remaining CO ligands are rearranged to give a near octahedral geometry about the Fe centre. The geometry optimisation of H_2:DP proceeds from $\{DP$-$H^{1-}\}$, where the additional H atom is place on the five-coordinate Fe centre and the CO ligands are rearranged to give an octahedral geometry about the Fe centre. Three geometrical isomers of DP-H_2 were calculated; an axial:equatorial isomer denoted as $\{eq\ DP$-$H_2\}$ and two axial:axial isomers (*cis*- and *trans*-forms) denoted as $\{cis\ DP$-$H_2\}$ and $\{trans\ DP$-$H_2\}$, respectively (Figure 4).
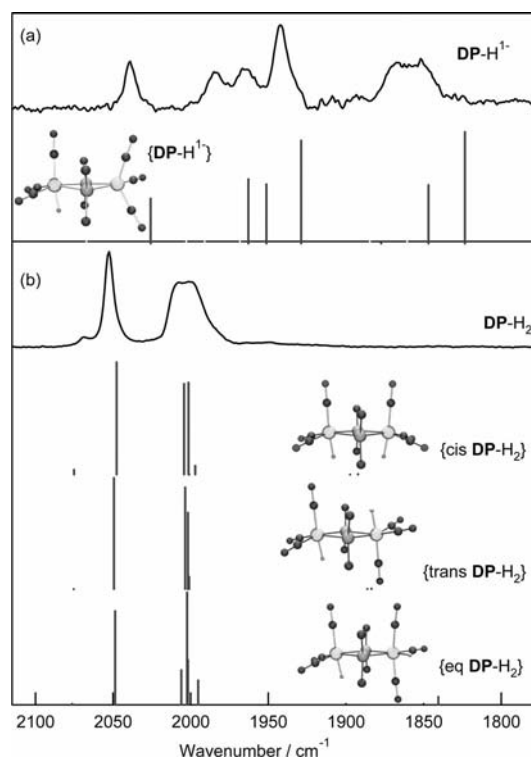

Figure 4. Observed (from ref.[10]) and DFT-calculated ν(CO) wavenumbers and relative intensities of (a) DP-H^{1-} and (b) DP-H_2. A scaling factor of 0.98 is applied to the frequencies calculated by DFT. DFT-optimised geometries of $\{DP$-$H^{1-}\}$ and the axial:axial isomers of $\{DP$-$H_2\}$. For clarity, the hydrogen atoms on the methyl groups are excluded.

Comparison between $\{DP^{2-}\}$ and the Crystallographic Structure

For comparison, selected bond lengths for the previously reported X-ray structure[21] and optimised geometry for $\{DP^{2-}\}$[10,22] are presented in Table 2. While there is close

agreement between the calculated and observed Fe–C and C–O distances and the planar Fe–P–P–Fe core geometry, poor numerical agreement is obtained for the non-bonding Fe–Fe and Fe–P distances, these being overestimated by 0.077 Å and 0.056 Å, respectively, relative to the crystallographic values.

Table 2. Structural parameters for {DP^{2-}}, {DP-H^{1-}} and {DP-H_2}.

| | {DP^{2-}}[10,22] | {DP-H^{1-}} | {DP-H_2} | | |
			trans[a]	*cis*	eq
ΔG[b]			0	0.48	3.94
Fe–Fe[c]	3.707 (3.630)[d]	3.657	3.633	3.633	3.631
Fe–P	2.336 (2.233)	2.329	2.327	2.327	2.341
Fe–CO	1.754 (1.750)	1.786 [1.763][e]	1.798	1.798	1.801
C–O	1.175 (1.164)	1.151 [1.167]	1.145	1.144	1.145
Fe–CO$_{trans}$	–	1.803	1.814	1.815	–
C–O$_{trans}$	–	1.15	1.145	1.145	–
P–P	2.864 (2.759)	2.875	2.908	2.906	2.955
Fe–H	–	1.526	1.527	1.524	1.527
H–H	–	–	4.244	3.104	4.709
Dihedral[f]	179.7 (180.0)	171.1	179.1	176.6	179.9

[a] The distances for {*trans* DP-H_2} are within 0.003 Å of those for the *cis* isomer, except for the H–H distance, which is 4.244 Å. [b] Calculated at 273.15 K in units of kcal mol^{-1}. [c] All distances in Å. [d] Crystallographic values, from ref.[21] [e] Fe–CO and CO distances for the CO groups on the Fe(CO)$_3$ fragment. [f] Fe–P–P–Fe dihedral angle in degrees (°).

{DP-H^{1-}}

Protonation of the 2Fe2P core is calculated to give a shortening of the Fe–Fe and Fe–P distances and a lengthening of the Fe–CO distances, particularly for the CO group *trans* to the hydride (Table 2). A small folding of the 2Fe2P core is also predicted to accompany protonation. The validity of the calculation of {DP-H^{1-}} is confirmed by the excellent agreement between the calculated ν(CO) IR spectrum for {DP-H^{1-}} with that observed for DP-H^{1-} (Figure 4a). Further, the calculated normal modes of the higher- and lower-wavenumber groups of bands are due to C–O stretching vibrations of the six-coordinate, protonated Fe(CO)$_3$ and five-coordinate Fe(CO)$_3$ subunits, respectively. The average value of the ν(CO) modes of the Fe(CO)$_3$ unit provide a measure of the electron-richness of the Fe centre, and the IR spectra clearly reflect the weak electronic communication between the Fe centres of DP-H^{1-}.

The absence of observable dihydrogen elimination following protonation of DP-H^{1-} is due to kinetic rather than thermodynamic factors. In this case, the Fe–H bond is slightly inclined toward the bridging diphenylphosphido groups, most likely due to steric interactions, making the site adjacent to the Fe–H group less accessible for protonation. In contrast, the terminally bound hydride of **4Fe6S**-H^{1-} or [2Fe]$_H$ is located *trans* to a bridging CO group and *cis* to the bridging dithiolates. This provides an open coor-

dination geometry adjacent to the Fe–H group, which would be expected to be more accessible for protonation.
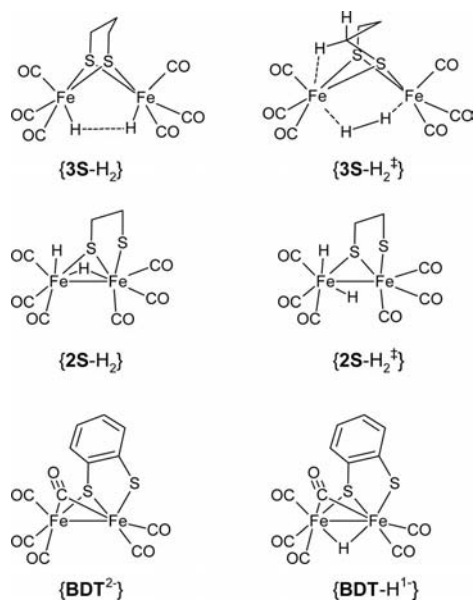
Isomeric Forms of {DP-H_2}

DFT geometry optimisation of {*cis* DP-H_2}, {*trans* DP-H_2} and {eq DP-H_2} proceed to well-defined minima with calculated energies in the order {*trans* DP-H_2} < {*cis* DP-H_2} << {eq DP-H_2}. These results are consistent with ^{31}P NMR spectra of DP-H_2[23] and ^{1}H NMR spectra of the (trifluoromethyl)phosphido-bridged analogue, [Fe(CO)$_3$]$_2$-{μ-P(CF$_3$)$_2$}$_2$ (DP_F-H_2),[24] which indicate a mixture of the *cis* and *trans* isomers of the axial:axial form and no observable axial:equatorial isomer. Comparison between the observed and calculated IR spectra for both the *cis*- and *trans*- isomers of {DP-H_2} is shown in Figure 4b. The calculated spectra of the {*cis* DP-H_2} and {*trans* DP-H_2} isomers are almost indistinguishable (Figure 4b), consequently the predominant form cannot be identified on the basis of the IR spectra.

The interatomic distances of the *cis* and *trans* isomers of {DP-H_2} are similar (Table 2) and described together as follows. The calculated Fe–Fe distance is 3.633 Å and is in close agreement with the XAFS-derived value of 3.62 Å. The calculated Fe–P distance is overestimated by 0.067 Å relative to the XAFS-derived value, this discrepancy being similar to that obtained for the corresponding contacts of DP, and the related **3P** redox series.[14] The calculated Fe–H distances for the two isomers of {DP-H_2} are 1.524 (*cis*) and 1.527 Å (*trans*), which are longer than the XAFS-estimated value (Table 1). Given the uncertainty in extracting meaningful Fe–H distance from the XAFS analysis, discussed earlier, the difference is not considered significant. Moreover, the DFT-calculated Fe–H distances are in agreement with the crystallographically determined value for AH_t^+ [1.52(4) Å].[6] The calculated Fe–C(O) distances reflect the coordination environment around the Fe centres, where the *trans* influence of the hydride ligand is reflected by the calculated Fe–C$_{trans}$(O) and Fe–C(O) distances (Table 2). While following the same trend obtained from the XAFS analysis (Table 1), the magnitude of the calculated difference in bond lengths is smaller than that inferred from XAFS. While the discrepancy between the *cis* and *trans* Fe–C(O) distances may be due to aspects of the calculation (e.g. functional and basis set selection), we defer exploring these aspects of the calculations until XAFS analyses over a more extended *k* range are available. In its present configuration, BL20B is not well suited to the collection of such data.

Dihydrogen Elimination from DP-H$_2$

The driving force for proton reduction by DP^{2-} can be estimated by the difference in reduction potentials for the DP/DP^{2-} and H$^+$/H$_2$ couples, which is approximately 1.5 V in CH$_3$CN. The calculated energy difference between {*cis* DP-H_2} and a non-interacting mixture of {DP} and {H$_2$} molecules confirm a large driving force (9.61 kcal mol^{-1}) for the reaction from the dihydride intermediate. The kinetic factors responsible for the failure of DP^{2-} to reduce protons may be considered in the context of the calculated struc-

tures of the protonated forms and the suggested reaction paths for the thiolato-bridged analogues (Scheme 1). Should proton reduction proceed through a path analogous to that of **3S**, then the dihydride intermediate would be accessible, corresponding to {*cis* **DP**-H$_2$}; however, the geometry of the 2Fe2P core dictates a large H–H separation (3.104 Å), and the transition state with a dihydrogen bridge between two iron atoms is not tenable. The alternative reaction path, analogous to that of **2S**, has a transition state that could be more readily accommodated with structures having a long Fe–Fe distance; however, the intermediate dihydride leading to the transition state has a bridging hydride, and this is not tenable for a species with an Fe–Fe distance much greater than 3 Å [cf. (**DP**-H^{1-})].

Scheme 1. Calculated intermediates and transition states for dihydrogen elimination from the two-electron, two-proton analogues of **2S** and **3S** together with the calculated geometries of **BDT**$^{2-}$ and **BDT**-H^{1-}.

Isomeric Forms of {3P-H$_2$}

As previously discussed,[14] the doubly protonated forms of **3P**$^{2-}$ present additional complexity owing to the inequivalence of the axial coordination sites, thus the axial:axial form has three isomers, designated up:up, up:down and down:down according to whether the axial site is adjacent or opposite the propylene linker and two isomers of the axial:equatorial form designated eq:up and eq:down. Since electrocatalytic proton reduction is central to this investigation, the DFT calculations of the three axial:axial isomers and the axial:equatorial isomer with the closest H–H approach ({eq:down **3P**-H$_2$}) are summarised in Figure 5. The Fe–P–P–Fe dihedral angle varies between 136.5 ({eq:down **3P**-H$_2$}) and 141.0° ({up:up **3P**-H$_2$}), indicating a degree of flexibility of the 2Fe2P core geometry. Most importantly, only {down:down **3P**-H$_2$} gives a geometry that would access a transition state for dihydrogen elimination analogous to that of {**3S**-H$_2$‡}, and in this case the isomer is

2.63 kcal mol^{-1} higher than the isomer with the lowest energy. The calculated spectra of the different isomers of **3P**-H$_2$ are given in Figure 5 and compared with those of a short-lived product identified as **3P**-H$_2$ obtained from previous IR spectroelectrochemical studies of **3P** and HOTs.[14] The predicted IR spectrum most closely matching that of **3P**-H$_2$ corresponds to the lowest-energy isomer, {up:down **3P**-H$_2$}, or a mixture of up:up and up:down isomers. These isomers have a long H–H separation and may be expected to be unproductive with respect to dihydrogen elimination and could therefore be generated in an observable standing concentration. The loss of the **3P**-H$_2$ spectrum at the end of the spectroelectrochemical reaction may be explained either in terms of rearrangement to the reactive down:down form or the reduction of these species at the end of the reaction.
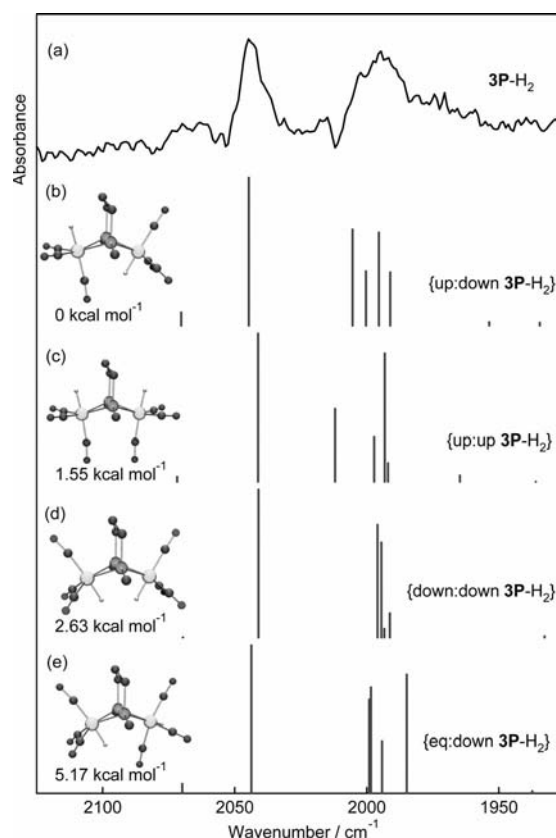

Figure 5. (a) Spectrum attributed to **3P**-H$_2$[14] and (b–e) DFT-calculated structures, relative energies (298.15 K) and ν(CO) wavenumbers and relative intensities of the isomers of **3P**-H$_2$.

Modelling of Electrocatalytic Proton Reduction

While satisfactory modelling of the voltammetric response obtained from solutions of **2S**,[25] **3S**[15] and **3P**[14] with HOTs have been reported, those studies have not delineated the range of rate constants for the elimination of dihydrogen from the two-electron reduced species compatible with the experimental data. Further, the recent calculations of the reaction path for electrocatalytic proton reduction by

2S provide thermodynamic and kinetic parameters[12] that can be referenced to the experimental results. The sequence of redox and protonation steps leading to electrocatalytic proton reduction in the presence of strong acids, deduced from analysis of the electrochemical results, is shown in Scheme 2. While DFT calculations broadly support the reaction path, they also suggest equilibria between isomeric forms of **2S**-H^{1-} and **2S**-H$_2$, although these details will not be evident in the electrochemical response.
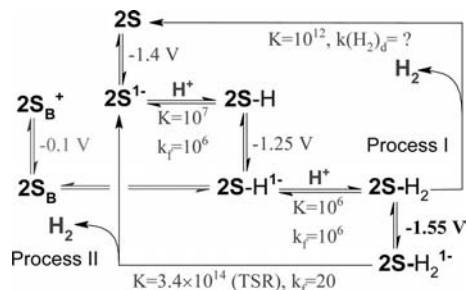
Scheme 2. Reaction path for electrocatalytic proton reduction by **2S**. With the exception of E^0(**2S**-H$_2$/**2S**-H$_2$$^{1-}$), the values of the equilibrium constants and reduction potentials have been adjusted from the previous report[25] to values suggested by DFT calculations.[12]

The cyclic voltammetry of CO-saturated THF solutions of **2S** with varying concentrations of HOTs (Figure 5a) is used to assess the modelling of the electrocatalytic reaction. The voltammetry for this catalyst/substrate combination is relatively simple with two electrocatalytic waves and no observable features associated with electrocatalysis by different reduction products. Moreover, the cyclic voltammetry of **2S** is more reversible for CO-saturated solutions, and there is no observable difference in the response obtained for solutions of **2S** and HOTs saturated with Ar or CO.

As has recently been noted,[26] a characteristic of electrochemical simulations is that for favourable equilibria the computed response is highly sensitive to the kinetics but insensitive to the magnitude of the equilibrium constants. For example, the K_b values of **2S**$^{1-}$ and **2S**-H^{1-} used for electrochemical modelling were 10 and 100, respectively, which are significantly lower than the calculated values (10^7 and 10^6). Apart from E^0(**2S**-H$_2$/**2S**-H$_2$$^{1-}$), where the value based on the DFT calculations (–1.45 V) gives too small a separation of the current response for Processes I and II, equilibrium constants and relative reduction potentials derived from the DFT analysis were used for the revised electrochemical modelling.

While the DFT calculations provide good estimates of the relative energies of alternative products or intermediate species, deduction of the reaction path presents significantly greater challenges. Our investigations of the alternative rate constants suggest that the rate constants for the protonation reactions, and associated structural rearrangements, are required to be relatively fast and not rate-limiting in order to reproduce the dependence of the voltammetry on HOTs concentration. Consistent with the previous electrochemical and DFT studies, dihydrogen elimination is rate-

limiting, and the calculated activation energies for dihydrogen elimination from **2S**-H$_2$ and **2S**-H$_2$$^{1-}$ (10.43 and 4.26 kcal mol^{-1})[5] are consistent with the observed higher rate of electrocatalysis for the more reduced species.

Experimentally, the current response for Process I becomes saturated when the concentration of HOTs reaches approximately 5 equiv. relative to that of **2S**; thereafter Process II dominates (Figure 6). Electrochemical simulations based on Scheme 2 show that the current response for Process I is insensitive to the equilibrium constant for dihydrogen elimination from **2S**-H$_2$, so long as the value is larger than 1, but is sensitive to the rate of dihydrogen elimination [k(H$_2$)$_d$] from **2S**-H$_2$. As shown in Figure 6, a rate constant of 6 s^{-1} gives a peak current that saturates with [HOTs] greater than 5 mM at a value approximately three times that obtained from the 1 mM solution of **2S** in the absence of acid. Based on the simulations obtained with higher and lower values of the rate constant (Figure 6b, d), a rate in the range 4–8 s^{-1} for k(H$_2$)$_d$ from **2S**-H$_2$ is obtained. Despite the very different values of many of the equilibrium constants, this value is in agreement with the previous analysis.[25] The value of the rate of dihydrogen elimination from **2S**-H$_2$$^{1-}$ was adjusted to give the closest match be-
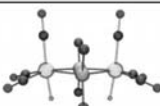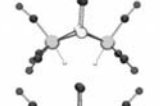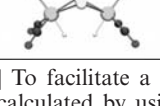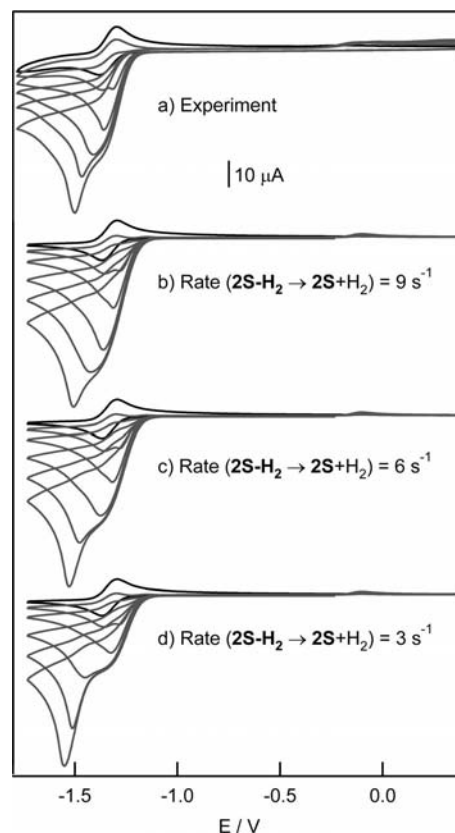

Figure 6. Observed and calculated cyclic voltammetry of 1 mM solutions of **2S** with 0, 1, 2.5, 5, 7.5 and 10 mM HOTs. (a) Experimental: 2 mm diameter reticulated vitreous carbon working, Pt counter and Ag pseudo-reference electrodes, CO-saturated THF; 0.2 M [Bu$_4$N][PF$_6$] supporting electrolyte. (b–d) Calculated: thermodynamic and kinetic parameters as summarised in Scheme 2 where the rate of dihydrogen elimination from **2S**-H$_2$ is varied between 3 and 9 s^{-1}.

tween the observed and calculated current response. Since this process is dependent on the preceding dihydrogen elimination step, the rate constant cannot be restricted to as narrow a range of values and a satisfactory current response can be obtained with rates of dihydrogen elimination from $2S$-H_2^{1-} between 20 and 100 s^{-1}.

The simulations of electrocatalytic proton reduction of HOTs by $3S$ and $3P$ have also been reviewed so as to include DFT-based estimates of the pK_a values of the one-electron, one-proton and two-electron, two-proton species and ΔG_r for elimination of H_2 by Process I; these are available as Supporting Information. As in the case of $2S$, equally good or improved modelling of the experimental results is obtained without significant change in $k(H_2)_d$ (Table 3).

Table 3. Comparison between values of $k(H_2)_d$ obtained from electrochemical studies and the calculated H–H distance for the down:down isomers of {DP-H_2}, {$3P$-H_2}, {$3S$-H_2} and {$2S$-H_2}.

	$k(H_2)_d$ / s^{-1}	$r(H{-}H)$ / Å
{DP-H_2}	~ 0	3.104
{$3P$-H_2}	1.5-4[b]	2.067
{$3S$-H_2}[a]	2-7[b]	1.886
{$2S$-H_2}	4-8[b]	1.852

[a] To facilitate a direct comparison, the structure of {$3S$-H_2} is recalculated by using the same methods as those of {$3P$-H_2}. [b] Revised estimates based on data from ref.[14] ($3P$) and ref.[15] ($3S$).

Dihydrogen Elimination from $3P$-H_2

Previous investigations have shown that the 2Fe2P core geometry can be modified by linking the P atoms, impacting on the geometry both of $3P^{2-}$ and the protonated species. Most importantly, $3P^{2-}$ reduces protons and catalyses proton reduction at the two-electron level with rate-limiting dihydrogen elimination analogous to $3S$, although with approximately half the rate (Table 3). It was previously noted that $k(H_2)_d$ for $3S$-H_2, $3P$-H_2 and DP-H_2 is inversely related to the calculated H–H distance for the different species (Table 3) and that this would be readily explained in terms of the reaction path proposed for $3S$ (Scheme 1). However, in light of the alternative reaction path proposed for $2S$, it should also be noted that folding of the 2Fe2P core, resulting from the propylene linker for $3P^{2-}$, may also increase the stability of the hydride-bridged intermediate, allowing formation of the transition state proposed for $2S$ (Scheme 1). The feasibility of such a reaction path depends on the potential of a hydride-bridged form of $3P$-H^{1-}. DFT geometry optimisation of $3P$-H^{1-} proceeds to give terminally bound hydride structures analogous to that of {DP-H^{1-}}, irrespective of the initial placement of the hydrogen atom.[14] Evidently, the Fe–Fe distance is just too long to favour formation of a bridged hydride. In this event, dihydrogen elimination from a dihydride analogous to {$2S$-$H_2^{\ddagger}$} would require protonation of {$3P$-H^{1-}} at the six-coordinate iron centre. However, as is evident from the IR spectra of DP-H^{1-}, that iron centre is less electron rich and protonation of the five-coordinate iron would be favoured, as illustrated by the formation of DP-H_2. This conclusion is supported by the observation of up:up and up:down isomers of $3P$-H_2 in SEC studies during electrocatalytic proton reduction. Hence, it is highly unlikely that dihydrogen elimination from $3P$-H_2 would proceed from a transition state analogous to {$2S$-$H_2^{\ddagger}$}.

While dihydrogen elimination from a transition state related to down:down $3P$-H_2 is strongly implied by the foregoing discussion, the stabilisation of the transition state by the methylene protons of the bridge implied by {$3S$-$H_2^{\ddagger}$} carries significantly greater steric and conformational penalties for $3P$-H_2. Moreover, the relative energies of the isomeric forms of $3S$-H_2 and $3P$-H_2 are likely to be different as a consequence of the smaller Fe–X–X–Fe dihedral angle expected for S (133.9° for {$3S$-H_2}). In this context, the close agreement between the rates of dihydrogen elimination from $2S$, $3S$ and $3P$ is surprising, a point amplified by modelling of strong acid electrocatalysis by [Fe(CO)$_3$]$_2$-{μ-SCH$_2$N(CH$_2$CH$_2$OCH$_3$)CH$_2$S} ($3SN$).[26] While the potential of the electrocatalytic reaction is affected by protonation of the azadithiolate bridge, the rate of dihydrogen elimination from $3SN$-H_2 is rate-limiting and is estimated to be 3 s^{-1}, i.e. similar to $2S$, $3S$ and $3P$.

Conclusions

The rates of electrocatalytic proton reduction by diiron compounds related to [2Fe]$_H$ are governed by dihydrogen formation and elimination from the metal centre. Two distinct reaction paths may be discerned; reaction from a single metal centre evolving from a terminally bound hydride or involvement of both metal centres through the agency of a bridging metal hydride.[11,27] While it is generally believed that the terminally bound hydrides are more reactive, the failure of DP-H^{1-} to give observable reaction when treated with strong acid is surprising. DFT and IR spectroscopy of the short-lived DP-H^{1-} species suggest that the two iron centres weakly interact and electronic and steric effects make further protonation of the protonated octahedral iron centre uncompetitive with the formation of DP-H_2. For both [2Fe]$_H$ and $4Fe6S$, the reactive terminally bound hydride is *trans* to a bridging CO group and *cis* to the bridging thiolato groups, and this leads to a less sterically congested coordination site adjacent to the terminally bound hydride.

The previously reported IR spectra and DFT calculations[10] of DP-H_2 are supplemented by structural details extracted from XAFS analysis. While the Fe–H interaction is not well characterised by those measurements, secondary

effects on the coordination environment of the iron centre resulting from the strong *trans* influence of the hydride ligand are apparent. The stability of **DP**-H$_2$ with respect to dihydrogen elimination is readily understood in terms of the large H–H separation relative to that calculated for **3P**-H$_2$ and **3S**-H$_2$.

DFT calculation of the reaction path for dihydrogen elimination from bridged hydrides has been reported for **2S**[12] and **3S**, in which the intermediates suggested for the two cases being markedly different (Scheme 1), with limiting descriptions of the dithiolate-S atoms either both bridging ({**3S**-H$_2$}) or having bridging and terminally bound forms ({**2S**-H$_2$}). The rate of dihydrogen elimination from the respective two-electron, two-proton species has been re-examined with inclusion of estimates of the equilibrium constants and reduction potentials deduced from the DFT calculations. The $k(H_2)_d$ values that allow satisfactory reproduction of the observed response are similar for **2S**-H$_2$, **3S**-H$_2$ and **3P**-H$_2$, an observation seemingly inconsistent with the calculated reaction path for **2S** and **3S**. The observation that electrocatalysis is obtained at the two-electron level for **3P** and not **DP**, together with consideration of the 2Fe2P core geometry, suggests that dihydrogen formation and elimination requires involvement of both Fe atoms. While this conclusion implies that the transition state for these reactions more closely resembles {**3S**-H$_2$} than {**2S**-H$_2$}, the very similar values of $k(H_2)_d$ that apply to **3P**, **3S** and **2S** remain a challenge for the computational analysis of the reaction.

DFT calculations provide important insights into the chemistry of [2Fe]$_H$ analogues,[28] and this is reflected by the comparisons of the structural parameters and IR spectra of the protonated, reduced compounds examined herein. Further, the calculated values of equilibrium constants and reduction potentials derived from the relative energies of intermediate species can significantly enhance electrochemical modelling of complex electrocatalytic reactions. However, the identification of the transition state for more complex molecules presents significant challenges, and there remains much room for improvement in the range and quality of experimental measurements and their use to validate the computational studies.

Experimental Section

General Remarks

Samples of **DP** were prepared by using literature methods[29] and confirmed to be pure by spectroscopic and electrochemical analyses. Samples of *p*-toluenesulfonic acid, HOTs, (Merck) were obtained from commercial sources and used without further purification. High-purity argon and nitrogen were obtained from BOC gases. Solvents were dried by using standard procedures[30] and distilled under an atmosphere of dinitrogen immediately prior to use. The tetra-*n*-butlyammonium hexafluorophosphate (TBA[PF$_6$]) used for electrochemical measurements was synthesised and purified by using standard procedures.[31]

Continuous flow electrosynthesis experiments were conducted by using a cell described in the literature,[32] which incorporates reticu-

lated vitreous carbon as the working and counter electrodes and a jacketed silver wire as pseudo-reference electrode. Standard liquid chromatography fittings in conjunction with narrow-bore (0.2 mm i.d.) Teflon tubing was used to transfer solutions from the syringe pump to the electrosynthesis cell and then to the sample cells. The extent of electrosynthesis was monitored by IR spectroscopy.

Instrumentation: IR SEC spectra were collected by using a Biorad FT175C FTIR with Ge/KBr beamsplitter and narrow band MCT detector. Spectral subtraction and curve fitting was performed with Grams/32 AI software (Galactic). Multicomponent analysis was conducted by using routines available within the program Igor Pro (version 5.04B, Wavemetrics). A Bruker ECS106 X-band spectrometer was used to collect EPR spectra.

XAFS Sample Preparation and Analysis: Fe K-edge (7111.2 eV) X-ray absorption measurements were conducted by using the bending magnet source of beamline 20B at the KEK Photon Factory Tsukuba, Japan. A channel cut Si(111) monochromator with energy resolution ($\Delta E/E$) of approximately 2.4×10^{-4} provided the source of monochromatic radiation, where higher-order harmonics at the selected wavelength were rejected by detuning the monochromator by a factor of one half. Solutions were measured in the fluorescence mode by using a 36 element Ge detector (Canberra). Data analysis was conducted with the XFIT suite of programs,[33] which incorporates *FEFF ver. 6.01*.[34] Details of the procedures followed for the analysis of related systems have been described previously.[20,35] Samples of the reduced compounds were generated by continuous-flow electrosynthesis with 5 mM (i.e. 10 mM in Fe) solutions of **DP** in THF/0.2 M TBA[PF$_6$]. The potential of the cell was controlled with a PAR model 273A potentiostat, and the composition of the solution was monitored, in line, by IR spectroscopy (Shimadzu, Prestige). The sample was freeze-quenched in liquid nitrogen.

DFT Calculations

All reported calculations were conducted by using the hybrid functional B3LYP as implemented in the Gaussian 03 (G03, revision B.04) package[36] using the all-electron basis set 6-311+G(d) with diffuse and polarisation functions from the internal library of G03. Calculations were conducted for the spin singlet form on an analogue of **DP** in which the phenyl rings were replaced by methyl groups. This simplification reduced significantly the time needed for the calculations to reach convergence. While a similar outcome may have been obtained by restricting the conformational freedom of the phenyl rings, previous calculations[22] suggest that methyl substitution provides a satisfactory alternative. The calculated analogue of **DP** is designated {**DP**}, where the parentheses designate a DFT calculated species. Vibrational analyses were carried out as second derivatives and confirm that all optimised geometries were true minima.

Solvation effects were included by using the PCM model[37] as implemented in G03 with THF as the implicit solvent. Molecular cavities were built as solvent-excluding surfaces with the United Atom Topological Model and atomic radii optimised for the PBE0/6-31G(d) level of theory. All final geometry optimisations and subsequent vibrational analyses were conducted within the PCM framework described above.

Supporting Information (see footnote on the first page of this article): XANES of **DP**, **DP**$^{2-}$ and **DP**-H$_2$, details of the reaction scheme parameters and plots for electrochemical simulations of **2S**, **3S** and **3P**.

Acknowledgments

[1] R. Cammack, M. Frey, R. Robson, *Hydrogen as a Fuel: Learning from Nature*, Taylor & Francis Ltd., London, **2001**.

[2] K. A. Vincent, A. Parkin, F. A. Armstrong, *Chem. Rev.* **2007**, *107*, 4366–413.

[3] a) C. Tard, C. J. Pickett, *Chem. Rev.* **2009**, *109*, 2245–74; b) B. E. Barton, M. T. Olsen, T. B. Rauchfuss, *Curr. Opin. Biotechnol.* **2010**, *21*, 292–297; c) F. Gloaguen, T. B. Rauchfuss, *Chem. Soc. Rev.* **2009**, *38*, 100–108; d) J.-F. Capon, F. Gloaguen, F. Y. Petillon, P. Schollhammer, J. Talarmin, *Coord. Chem. Rev.* **2009**, *253*, 1476–94; e) M. L. Singleton, N. Bhuvanesh, J. H. Reibenspies, M. Y. Darensbourg, *Angew. Chem.* **2008**, *120*, 9634; *Angew. Chem. Int. Ed.* **2008**, *47*, 9492–9495.

[4] a) M. H. Cheah, C. Tard, S. J. Borg, X. Liu, S. K. Ibrahim, C. J. Pickett, S. P. Best, *J. Am. Chem. Soc.* **2007**, *129*, 11085–92; b) C. Tard, X. Liu, D. L. Hughes, C. J. Pickett, *Chem. Commun.* **2005**, 133–135.

[5] P. Surawatanawong, M. B. Hall, *Inorg. Chem.* **2010**, *49*, 5737–47.

[6] J. I. van der Vlugt, T. B. Rauchfuss, C. M. Whaley, S. R. Wilson, *J. Am. Chem. Soc.* **2005**, *127*, 16012–16013.

[7] B. E. Barton, T. B. Rauchfuss, *Inorg. Chem.* **2008**, *47*, 2261–2263.

[8] a) B. E. Barton, G. Zampella, A. K. Justice, L. De Gioia, T. B. Rauchfuss, S. R. Wilson, *Dalton Trans.* **2010**, *39*, 3011–3019; b) S. Ezzaher, J.-F. Capon, F. Gloaguen, F. Y. Petillon, P. Schollhammer, J. Talarmin, N. Kervarec, *Inorg. Chem.* **2009**, *48*, 2–4; c) N. Wang, M. Wang, T. Zhang, P. Li, J. Liu, L. Sun, *Chem. Commun.* **2008**, 5800–5802; d) X. Zhao, I. P. Georgakaki, M. L. Miller, R. Mejia-Rodriguez, C.-Y. Chiang, M. Y. Darensbourg, *Inorg. Chem.* **2002**, *41*, 3917–28.

[9] S. Ezzaher, J.-F. Capon, F. Gloaguen, F. Y. Petillon, P. Schollhammer, J. Talarmin, R. Pichon, N. Kervarec, *Inorg. Chem.* **2007**, *46*, 3426–3428.

[10] M. H. Cheah, S. J. Borg, M. I. Bondin, S. P. Best, *Inorg. Chem.* **2004**, *43*, 5635–44.

[11] G. Zampella, C. Greco, P. Fantucci, L. De Gioia, *Inorg. Chem.* **2006**, *45*, 4109–18.

[12] P. Surawatanawong, J. W. Tye, M. Y. Darensbourg, M. B. Hall, *Dalton Trans.* **2010**, *39*, 3093–104.

[13] G. A. N. Felton, A. K. Vannucci, J. Chen, L. T. Lockett, N. Okumura, B. J. Petro, U. I. Zakai, D. H. Evans, R. S. Glass, D. L. Lichtenberger, *J. Am. Chem. Soc.* **2007**, *129*, 12521–30.

[14] M. H. Cheah, S. J. Borg, S. P. Best, *Inorg. Chem.* **2007**, *46*, 1741–50.

[15] S. J. Borg, T. Behrsing, S. P. Best, M. Razavet, X. Liu, C. J. Pickett, *J. Am. Chem. Soc.* **2004**, *126*, 16988–99.

[16] C. Greco, G. Zampella, L. Bertini, M. Bruschi, P. Fantucci, L. De Gioia, *Inorg. Chem.* **2007**, *46*, 108–16.

[17] a) J.-F. Capon, F. Gloaguen, F. Y. Petillon, P. Schollhammer, J. Talarmin, *Eur. J. Inorg. Chem.* **2008**, 4671–81; b) T. B. Rauchfuss, *Angew. Chem. Int. Ed.* **2010**, *49*, 4166–4168.

[18] E. A. Stern, *Phys. Rev. B* **1993**, *48*, 9825–9827.

[19] a) G. Guilera, G. S. McGrady, J. W. Steed, R. P. L. Burchell, P. Sirsch, A. J. Deeming, *New J. Chem.* **2008**, *32*, 1573–81; b) M. P. Rabalo, A. P. S. Teixeira, M. H. Garcia, d. P. M. F. Minas, M. T. Duarte, A. R. Dias, J. Campo, W. Wenseleers, E. Goovaerts, *Eur. J. Inorg. Chem.* **2006**, 2175–85; c) V. Arion, J.-J. Brunet, D. Neibecker, *Inorg. Chem.* **2001**, *40*, 2628–30.

[20] M. I. Bondin, S. J. Borg, M. H. Cheah, G. Foran, S. P. Best, *Aust. J. Chem.* **2006**, *59*, 263–272.

[21] R. E. Ginsburg, R. K. Rothrock, R. G. Finke, J. P. Collman, L. F. Dahl, *J. Am. Chem. Soc.* **1979**, *101*, 6550–6562.

[22] M.-H. Baik, T. Ziegler, C. K. Schauer, *J. Am. Chem. Soc.* **2000**, *122*, 9143–54.

[23] S. G. Shyu, A. Wojcicki, *Organometallics* **1985**, *4*, 1457–1459.

[24] R. C. Dobbie, D. Whittaker, *J. Chem. Soc. C* **1970**, 796–797.

[25] S. J. Borg, S. K. Ibrahim, C. J. Pickett, S. P. Best, *C. R. Chim.* **2008**, *11*, 852–60.

[26] J.-F. Capon, S. Ezzaher, F. Gloaguen, F. Y. Petillon, P. Schollhammer, J. Talarmin, *Chem. Eur. J.* **2008**, *14*, 1954–64.

[27] P. E. M. Siegbahn, J. W. Tye, M. B. Hall, *Chem. Rev.* **2007**, *107*, 4414–35.

[28] a) J. W. Tye, M. Y. Darensbourg, M. B. Hall, *Inorg. Chem.* **2008**, *47*, 2380–2388; b) J. W. Tye, M. Y. Darensbourg, M. B. Hall, *J. Comput. Chem.* **2006**, *27*, 1454–62; c) C. Greco, M. Bruschi, P. Fantucci, L. De Gioia, *J. Organomet. Chem.* **2009**, *694*, 2846–53.

[29] J. P. Collman, R. K. Rothrock, R. G. Finke, E. J. Moore, F. Rose-Munch, *Inorg. Chem.* **1982**, *21*, 146–56.

[30] R. J. Errington, *Guide to Practical Inorganic and Organo-Metallic Chemistry*, Blackie Academic & Professional, London, **1997**.

[31] D. T. Sawyer, A. Sobkowiak, J. J. L. Roberts, *Electrochemistry for Chemists*, Wiley-Interscience, New York, **1995**, 2nd. ed..

[32] M. I. Bondin, G. Foran, S. P. Best, *Aust. J. Chem.* **2001**, *54*, 705–709.

[33] a) P. J. Ellis, in *Xfit for Windows 95*, Australian Synchrotron Research Program, Sydney, **1996**; b) P. J. Ellis, H. C. Freeman, *J. Synchrotron Radiat.* **1995**, *2*, 190–195.

[34] S. I. Zabinsky, J. J. Rehr, A. Ankudinov, R. C. Albers, M. J. Eller, *Phys. Rev. B* **1995**, *52*, 2995–3009.

[35] a) M. H. Cheah, S. J. Borg, M. I. Bondin, S. P. Best, *Inorg. Chem.* **2004**, *43*, 5635–44; b) S. J. Borg, T. Behrsing, S. P. Best, M. Razavet, X. Liu, C. J. Pickett, *J. Am. Chem. Soc.* **2004**, *126*, 16988–99.

[36] M. J. Frisch, G. W. Trucks, H. B. Schlegel, G. E. Scuseria, M. A. Robb, J. R. Cheeseman, J. Montgomery, J. A. T. Vreven, K. N. Kudin, J. C. Burant, J. M. Millam, S. S. Iyengar, J. Tomasi, V. Barone, B. Mennucci, M. Cossi, G. Scalmani, N. Rega, G. A. Petersson, H. Nakatsuji, M. Hada, M. Ehara, K. Toyota, R. Fukuda, J. Hasegawa, M. Ishida, T. Nakajima, Y. Honda, O. Kitao, H. Nakai, M. Klene, X. Li, J. E. Knox, H. P. Hratchian, J. B. Cross, V. Bakken, C. Adamo, J. Jaramillo, R. Gomperts, R. E. Stratmann, O. Yazyev, A. J. Austin, R. Cammi, C. Pomelli, J. W. Ochterski, P. Y. Ayala, K. Morokuma, G. A. Voth, P. Salvador, J. J. Dannenberg, V. G. Zakrzewski, S. Dapprich, A. D. Daniels, M. C. Strain, O. Farkas, D. K. Malick, A. D. Rabuck, K. Raghavachari, J. B. Foresman, J. V. Ortiz, Q. Cui, A. G. Baboul, S. Clifford, J. Cioslowski, B. B. Stefanov, G. Liu, A. Liashenko, P. Piskorz, I. Komaromi, R. L. Martin, D. J. Fox, T. Keith, M. A. Al-Laham, C. Y. Peng, A. Nanayakkara, M. Challacombe, P. M. W. Gill, B. Johnson, W. Chen, M. W. Wong, C. Gonzalez, J. A. Pople, *Gaussian*, Inc., Wallingford CT, **2004**.

[37] a) R. Cammi, B. Mennucci, J. Tomasi, *J. Phys. Chem. A* **1999**, *103*, 9100–9108; b) R. Cammi, B. Mennucci, J. Tomasi, *J. Phys. Chem. A* **2000**, *104*, 5631–5637; c) B. Mennucci, E. Cances, J. Tomasi, *J. Phys. Chem. B* **1997**, *101*, 10506–17; d) B. Mennucci, J. Tomasi, *J. Chem. Phys.* **1997**, *106*, 5151–5158.

Received: October 15, 2010
Published Online: February 2, 2011